Biomaterials Science

ROYAL SOCIETY OF CHEMISTRY

PAPER

View Article Online
View Journal | View Issue

Cite this: *Biomater. Sci.*, 2023, **11**, 7387

Phosphorus core–shell tecto dendrimers for enhanced tumor imaging: the rigidity of the backbone matters†

Mengsi Zhan,‡[a,b] Dayuan Wang,‡[b] Lingzhou Zhao,‡[c] Liang Chen,[b] Zhijun Ouyang,[b] Serge Mignani,[d] Jean-Pierre Majoral,[e,f] Jinhua Zhao,*[c] Guixiang Zhang,*[a] Xiangyang Shi*[b,d] and Mingwu Shen*[b]

Nanoplatforms with amplified passive tumor targeting and enhanced protein resistance can evade unnecessary uptake by the reticuloendothelial system and achieve high tumor retention for accurate tumor theranostics. To achieve this goal, we here constructed phosphorus core–shell tecto dendrimers (CSTDs) with a *rigid* aromatic backbone core as a nanoplatform for enhanced fluorescence and single-photon emission computed tomography (SPECT) dual-mode imaging of tumors. In this study, the phosphorus P-G2.5/G3 CSTDs (G denotes generation) were partially conjugated with tetraazacyclododecane tetraacetic acid (DOTA), cyanine5.5 (Cy5.5) and 1,3-propane sulfonate (1,3-PS) and then labeled with ^{99m}Tc. The formed P-G2.5/G3-DOTA-Cy5.5-PS CSTDs possess good monodispersity with a particle size of 10.1 nm and desired protein resistance and cytocompatibility. Strikingly, compared to the counterpart material G3/G3-DOTA-Cy5.5-PS with both the core and shell components being *soft* poly(amidoamine) dendrimers, the developed P-G2.5/G3-DOTA-Cy5.5-PS complexes allow for more efficient cellular uptake and more significant penetration in 3-dimensional tumor spheroids *in vitro*, as well as more significant tumor retention and accumulation for enhanced dual-mode fluorescence and SPECT (after labelling with ^{99m}Tc) tumor imaging *in vivo*. Our studies suggest that the rigidity of the core for the constructed CSTDs matters in the amplification of the tumor enhanced permeability retention (EPR) effect for improved cancer nanomedicine development.

Received 19th July 2023,
Accepted 17th September 2023

DOI: 10.1039/d3bm01198d

rsc.li/biomaterials-science

Introduction

The continuous development of nanotechnology has contributed to the efficient diagnosis and treatment of tumors. It is vital to promote the accumulation of nanomaterials at tumor sites through active ligand-mediated targeting and the passive enhanced permeability retention (EPR) effect. On the one hand, nanomedicines modified with specific ligands such as folic acid,[1] phenylboronic acid,[2] LyP-1[3] and Arg-Gly-Asp peptide[4] can actively target tumors through ligand–receptor interactions, thus reducing the side effects to healthy tissues; on the other hand, most nanoplatforms such as dendrimers, liposomes, nanogels and micelles can accumulate at tumor sites through the passive EPR effect due to the large vascular cell gap of solid tumors with a dysfunctional lymphatic system.[5–7]

For EPR-based passive tumor targeting, a long-circulating nanomaterial with effective tumor transportation, which is strongly dependent on its size, shape, rigidity, surface charge and modification, is needed.[8–12] In particular, the size and rigidity of nanomaterials play a significant role in modulating their solid tumor penetration.[13] For example, our previous work has shown that core–shell tecto dendrimers (CSTDs) composed of a generation 5 (G5) poly(amidoamine) (PAMAM) dendrimer as a core and a G3 PAMAM dendrimer as a shell formed through supramolecular β-cyclodextrin (CD) and ada-

[a]*Department of Radiology, Shanghai Fourth People's Hospital, School of Medicine, Tongji University, Shanghai 200434, China. E-mail: guixiangzhang@sina.com*
[b]*State Key Laboratory for Modification of Chemical Fibers and Polymer Materials, Shanghai Engineering Research Center of Nano-Biomaterials and Regenerative Medicine, College of Biological Science and Medical Engineering, Donghua University, Shanghai 201620, China. E-mail: xshi@dhu.edu.cn, mwshen@dhu.edu.cn*
[c]*Department of Nuclear Medicine, Shanghai General Hospital, Shanghai Jiao Tong University School of Medicine, Shanghai 200080, China. E-mail: zhaojinhua1963@126.com*
[d]*CQM-Centro de Quimica da Madeira, Universidade da Madeira, Funchal 9020-105, Portugal*
[e]*Laboratoire de Chimie de Coordination du CNRS, 205 route de Narbonne, 31077 Toulouse Cedex 4, France*
[f]*Université Toulouse, 118 route de Narbonne, 31077 Toulouse Cedex 4, France*

†Electronic supplementary information (ESI) available: Full experimental details and additional experimental results. See DOI: https://doi.org/10.1039/d3bm01198d

‡These authors equally contributed to this work.

mantane (Ad) recognition (for short, G5-CD/Ad-G3) with a higher molecular weight and volume than the single generation G5 dendrimers have better 3-dimensional (3D) tumor spheroid permeability *in vitro* and a more enhanced EPR effect *in vivo* than the single G5 dendrimers.[14] Furthermore, liposomes with different stiffnesses and rigidities possess different tumor penetration and retention effects.[15] Dai *et al.* prepared liposomes with varied lengths and saturations of lipid chains to endow them with the same surface properties but different rigidities and found that the liposomes with stronger rigidity exhibited better cellular uptake tendency.[16] In another study, Jiang *et al.* constructed poly (lactic-*co*-glycolic acid) (PLGA)-lipid nanoparticles (P-L NPs) with a *rigid* structure that could be wrapped and internalized smoothly by HeLa cells, whereas the less *rigid* or *soft* PLGA-water-lipid NPs (P-W-L NPs) were less significantly wrapped and internalized by cells due to their significant deformation ability than the P-L NPs.[17] However, a systematic exploration of the EPR effect of other nanoplatforms with a more or less similar composition but varied degrees of rigidity is still lacking in the literature.

For EPR-based passive tumor targeting, it is also vital to reduce the clearance by the reticuloendothelial system (RES). NPs modified with hydrophilic groups such as polyethylene glycol,[18,19] cyclodextrins,[20] and zwitterions[21] can significantly escape the phagocytosis of the mononuclear macrophage system. Our previous work has shown that modification of zwitterions such as 1,3-propane sulfonate (1,3-PS), 2-methacryloyloxyethyl phosphorylcholine, and carboxymethylacrylamide on the surface of PAMAM dendrimers can endow them with improved antifouling property to boost therapeutic gene delivery and tumor multimodality imaging, thereby promoting the efficacy of the tumor theranostic effect.[22–24]

Dendrimers, characterized by highly branched and 3D structures, monodispersity, and abundant surface functional groups, have been paid much attention for the development of cancer theranostics. Compared with PAMAM dendrimers, phosphorus dendrimers have a more *rigid* structure and higher homogeneity in terms of molecular weight due to their unique internal structure and functional peripheral groups.[25–27] The emergence of CSTDs has contributed to a simplified synthesis process of high-generation dendrimers with improved gene/drug delivery efficiency.[28,29] In our previous work, we found that P-G2.5/G3 CSTDs formed with aldehyde-terminated G2.5 phosphorus dendrimers as the core and G3 PAMAM dendrimers as the shell could deliver plasmid DNA encoding enhanced green fluorescent protein or luciferase into tumor cells with a higher efficiency than the *soft* counterpart G3-CD/Ad-G3 CSTDs composed of G3 PAMAM dendrimers as both the core and shell due to the more *rigid* phosphorus dendrimer core of P-G2.5/G3 CSTDs featuring a stable backbone and a benzene ring structure to maintain an intact 3D structure with an enhanced DNA compaction ability.[30] However, few studies have explored the impact of the rigidity-influenced EPR effect of dendrimers on tumor imaging.

Some imaging techniques such as computed tomography, magnetic resonance, single-photon emission computed tomography (SPECT), positron emission tomography, and fluorescence imaging are crucial in the diagnosis of diseases such as malignant tumors, ischemic stroke, and cardiovascular diseases.[31–33] A combination of multiple imaging techniques can further improve the diagnostic accuracy of tumors and holds promise in personalized cancer therapy.[34] SPECT imaging has gained widespread attention because of its high sensitivity for functional imaging.[35,36] Herein, we constructed SPECT imaging contrast agents based on both *rigid* P-G2.5/G3 and *soft* G3-CD/Ad-G3 CSTDs with expected different tumor EPR effects. A fluorescent dye was also grafted onto the surface of both types of CSTDs to endow them with dual-mode fluorescence and SPECT imaging abilities. As shown in Scheme 1, both P-G2.5/G3 and G3-CD/Ad-G3 (G3/G3) CSTDs were synthesized according to our previous work,[14,30] conjugated with tetraazecyclododecane tetraacetic acid (DOTA), surface modified with cyanine5.5 (Cy5.5) and 1,3-PS, and further labeled with ^{99m}Tc to obtain the two different CSTD imaging agents, respectively. The constructed P-G2.5/G3-DOTA-Cy5.5-PS and G3/G3-DOTA-Cy5.5-PS CSTDs were well characterized, and their cytotoxicity, cellular uptake/3D tumor spheroid penetration abilities *in vitro*, and uses for dual-mode fluorescence/SPECT (after labelling with ^{99m}Tc) imaging of tumors *in vivo* were thoroughly investigated. To our knowledge, this is the first study associated with the impact of molecular rigidity of dendrimer platforms on their tumor EPR effect for tumor molecular imaging applications.

Experimental section

Preparation and characterization of P-G2.5/G3-DOTA-Cy5.5-PS and G3/G3-DOTA-Cy5.5-PS CSTDs

The P-G2.5/G3 CSTDs and G3-CD/Ad-G3 CSTDs (G3/G3 CSTDs) were synthesized according to the procedures described in our previous reports.[14,28,30] To synthesize P-G2.5/G3-DOTA CSTDs, a DMSO solution (5 mL) containing DOTA-NHS (3.13 mg) was dropwise added to a DMSO solution (5 mL) of P-G2.5/G3 CSTDs (30 mg) under stirring for 24 h. Then, a DMSO solution (5 mL) of Cy5.5 (2.94 mg) was dropwise added to the above mixture and stirred for 24 h at room temperature. After that, the reaction mixture was dialyzed against water (9 times, 2 L) for 3 days using a dialysis membrane with a molecular weight cut-off (MWCO) of 3500 and lyophilized to obtain the P-G2.5/G3-DOTA-Cy5.5 CSTDs. Afterwards, a water solution (5 mL) containing P-G2.5/G3-DOTA-Cy5.5 (25 mg) was mixed with an aqueous solution (5 mL) of 1,3-PS (1.4 mg) under stirring for 24 h. The reaction mixture was dialyzed and lyophilized to obtain the final product P-G2.5/G3-DOTA-Cy5.5-PS CSTDs. The synthesis process of G3/G3-DOTA-Cy5.5-PS CSTDs was the same as above. In brief, a DMSO solution (5 mL) containing DOTA-NHS (2.69 mg) was dropwise added to a DMSO solution (5 mL) of G3/G3 CSTDs (30 mg) under stirring for 24 h to obtain the G3/G3-DOTA CSTDs. Then, a DMSO solution (5 mL)

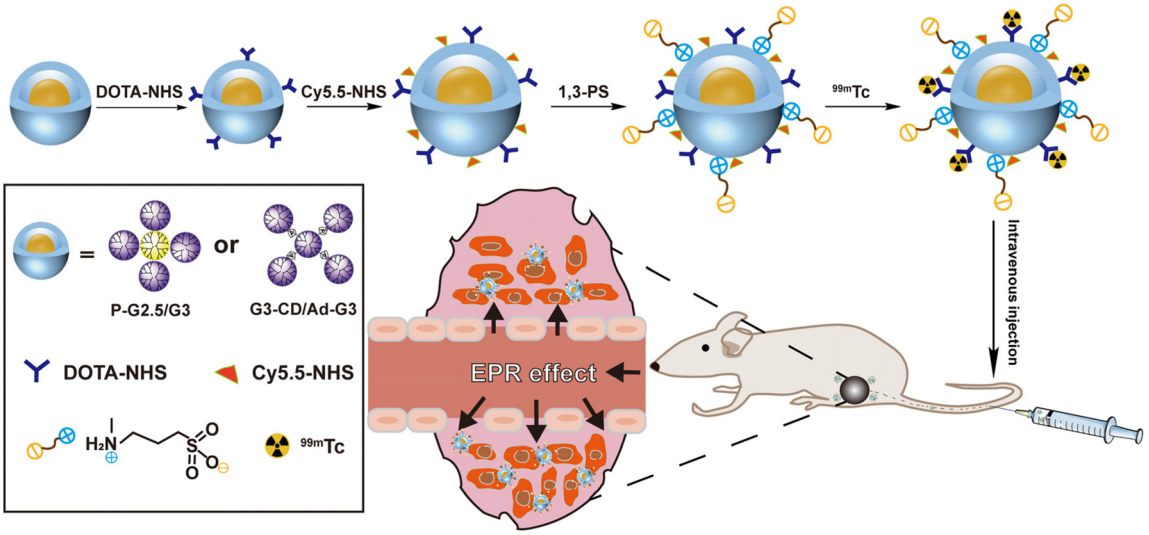

Scheme 1 Preparation of ^{99m}Tc-P-G2.5/G3-DOTA-Cy5.5-PS and ^{99m}Tc-G3/G3-DOTA-Cy5.5-PS complexes for dual-mode fluorescence/SPECT imaging of tumors.

of Cy5.5 (2.53 mg) was dropwise added to the above mixture while stirring at room temperature for 24 h. After that, the reaction mixture was dialyzed against water (9 times, 2 L) for 3 days using a dialysis membrane with a molecular weight cut-off (MWCO) of 3500 and lyophilized to obtain the G3/G3-DOTA-Cy5.5 CSTDs. Afterwards, a water solution containing G3/G3-DOTA-Cy5.5 (25 mg, 5 mL) was mixed with 1,3-PS (1.24 mg, in 5 mL water) under stirring for 24 h, and the reaction mixture was dialyzed and lyophilized to obtain the final product G3/G3-DOTA-Cy5.5-PS CSTDs. The formed CSTDs were thoroughly characterized by ^{1}H NMR, AFM, UV-vis spectroscopy, fluorescence spectroscopy, hydrodynamic size and zeta potential measurements, and protein resistance assay.

Cell culture and *in vitro* assays

B16 cells were regularly cultured, seeded and adopted for *in vitro* experiments including cytotoxicity assay, flow cytometry, confocal microscopy observation of cellular uptake, and tumor spheroid penetration of the P-G2.5/G3-DOTA-Cy5.5-PS and G3/G3-DOTA-Cy5.5-PS CSTDs.

Animal experiments

All animal experiments were performed following the protocols approved by the Animal Care and Use Committee of Donghua University (approval # DHUEC-STCSM-2021-03) and also in accordance with the policy of the National Ministry of Health of China. Male C57BL/6 mice (15–20 g, 4–6 week old, Shanghai Slac Laboratory Animal Center, Shanghai, China) were used to establish the subcutaneous melanoma tumor model and then utilized for *in vivo* experiments including fluorescence imaging, SPECT imaging, organ/tissue distribution, and histological examinations. See full experimental details in the ESI.†

Results and discussion

Synthesis and characterization of G3/G3-DOTA-Cy5.5-PS and P-G2.5/G3-DOTA-Cy5.5-PS CSTDs

The chemical structures of the G3 PAMAM dendrimer and G2.5 phosphorus dendrimer are shown in Fig. S1,† respectively. Both P-G2.5/G3 and G3-CD/Ad-G3 (G3/G3) CSTDs were synthesized according to our previous work,[14,30] partially modified with DOTA-NHS according to the literature[14] and characterized by ^{1}H NMR (Fig. S2†). The characteristic proton peaks at 2.2–3.4 ppm are attributed to the G3 PAMAM dendrimer, and they overlap with those of DOTA (Fig. S2A†).[14] In order to determine the amount of the attached DOTA moiety on the surface of G3/G3 CSTDs, the G3/G3-DOTA CSTDs were chelated with Gd(III) ions, and the number of Gd ions per CSTD was determined by inductively coupled plasma-optical emission spectrometry (ICP-OES) to be 4.2. Through an indirect method reported in the literature,[14] the number of DOTA moieties conjugated to each P-G2.5/G3 CSTD was deduced to be 4.1 (Fig. S2B†) due to the fact that the chelation of Gd(III) to the DOTA moiety is in a ratio of 1 : 1. In addition, the proton peaks at 1.89 ppm, 5.0 ppm, and 7.6–8.5 ppm are associated with 1,3-PS, β-CD, and the benzene ring, respectively. Based on the NMR integration, the number of 1,3-PS moieties modified on each G3/G3-DOTA and P-G2.5/G3-DOTA CSTD was calculated to be 19.1 and 19.3, respectively (Fig. S3†). Therefore, the two different CSTDs were modified with approximately equal amounts of DOTA and 1,3-PS, which is reasonable for subsequent comparison in biological performances.

In order to study the effect of the rigidity of the two different CSTDs on fluorescence imaging, the G3/G3-DOTA and P-G2.5/G3-DOTA CSTDs were modified with Cy5.5-NHS, respectively. As shown in Fig. S4 and S5,† both G3/G3-DOTA-Cy5.5 and P-G2.5/G3-DOTA-Cy5.5 CSTDs have an

obvious UV absorption peak at 690 nm, indicating the successful modification with Cy5.5. Meanwhile, the fluorescence intensities of G3/G3-DOTA-Cy5.5-PS and P-G2.5/G3-DOTA-Cy5.5-PS CSTDs were detected by fluorescence spectroscopy. Surprisingly, the fluorescence intensity of P-G2.5/G3-DOTA-Cy5.5 CSTDs is significantly stronger than that of the G3/G3-DOTA-Cy5.5-PS CSTDs at the same Cy5.5 concentration ([Cy5.5] = 5 μM). This may be attributed to the *rigid* structure of P-G2.5/G3-DOTA-Cy5.5 with benzene rings and double bonds that can block the molecular rotation, thus facilitating enhanced fluorescence emission (Fig. 1A).

By zwitterionic modification of 1,3-PS on the dendrimer surface, improved antifouling property is expected. As can be seen in Fig. 1B, the concentration of bovine serum albumin (BSA) in the supernatant was much higher in the P-G2.5/G3-DOTA-Cy5.5-PS group than in the P-G2.5/G3-DOTA group without 1,3-PS modification at the same CSTD concentrations, suggesting the excellent antifouling ability of P-G2.5/G3-DOTA-Cy5.5-PS. The same results can be observed in the G3/G3-DOTA-Cy5.5-PS group, as the G3/G3-DOTA-Cy5.5-PS CSTDs also show better protein resistance than the G3/G3-DOTA-Cy5.5 CSTDs without 1,3-PS modification.

We next characterized the size and morphology of G3/G3-DOTA-Cy5.5-PS and P-G2.5/G3-DOTA-Cy5.5-PS CSTDs. As shown in Table S1,† after modification with DOTA-NHS, Cy5.5-NHS, and 1,3-PS, the hydrodynamic size of the G3/G3-DOTA-Cy5.5-PS CSTDs significantly increased to 298.9 ± 14.7 nm, which is much larger than that of the pristine G3-CD/Ad-G3 CSTDs (207.9 ± 14.8 nm). Similarly, the P-G2.5/G3-DOTA-Cy5.5-PS CSTDs also have an increased hydrodynamic size of 176.8 ± 0.5 nm, which is larger than that of the P-G2.5/G3 CSTDs (144.5 ± 44.5 nm). The increased hydrodynamic size of the CSTDs implies their successful surface modifications. The zeta potential of G3/G3-DOTA-Cy5.5-PS or P-G2.5/G3-DOTA-Cy5.5-PS is lower than that of the respective materials due to the neutralization of the positively charged amine groups on the surface of the CSTDs after modifications with DOTA-NHS, Cy5.5-NHS, and 1,3-PS (Table S1†). The particle sizes and morphologies of the two CSTDs were observed by atomic force microscopy (AFM). As displayed in Fig. 1C and D, both types of CSTDs display a spherical shape. The heights of G3/G3-DOTA-Cy5.5-PS and P-G2.5/G3-DOTA-Cy5.5-PS were found to be 5.5 nm and 10.1 nm, respectively, which were increased by 0.7 nm and 0.3 nm compared with those of the pristine G3-CD/Ad-G3 and P-G2.5/G3 CSTDs, respectively.[30] This also suggests the successful modification of DOTA-NHS, Cy5.5 and 1,3-PS on their surface. It is noteworthy that despite the similar molecular dimensions of P-G2.5/G3 and G3-CD/Ad-G3 CSTDs, the P-G2.5/G3 (9.8 nm) shows a greater height profile than the G3-CD/Ad-G3 (4.8 nm), which is likely due to the rigid core of P-G2.5/G3 CSTDs that allows them to maintain an intact 3D molecular structure. In contrast, the G3-CD/Ad-G3 with a soft core has a structure that is prone to collapse after being dried, resulting in a lower height profile than that of the P-G2.5/G3. Furthermore, as shown in Fig. S6,† the hydrodynamic sizes of both G3/G3-DOTA-Cy5.5-PS and P-G2.5/

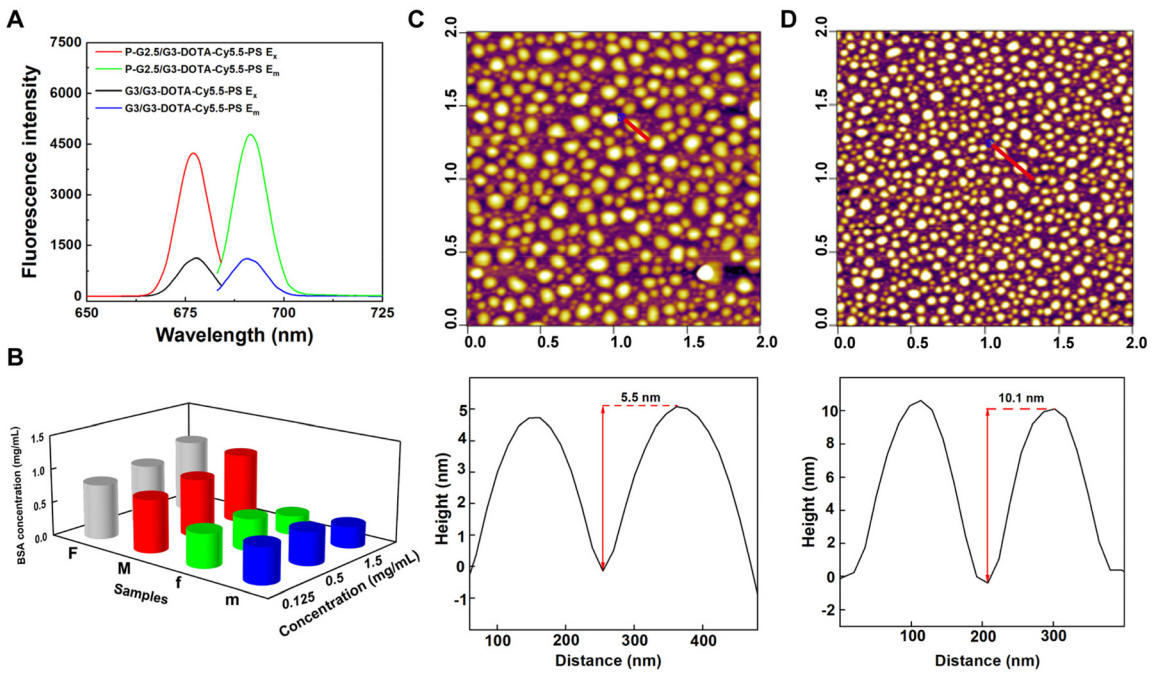

Fig. 1 (A) Fluorescence excitation spectra (left) and emission spectra (right) of P-G2.5/G3-DOTA-Cy5.5-PS and G3/G3-DOTA-Cy5.5-PS CSTDs at an excitation wavelength of 675 nm, respectively, at the same Cy5.5 concentration (5 μM). (B) The concentration of BSA in the supernatant after the samples of different concentrations (0.125, 0.5, and 1.5 mg mL^{-1}, respectively) were mixed with BSA and then centrifuged (F, M, f, and m represent P-G2.5/G3-DOTA-Cy5.5-PS, G3/G3-DOTA-Cy5.5-PS, P-G2.5/G3-DOTA-Cy5.5, and G3/G3-DOTA-Cy5.5, respectively). AFM images and height profiles of (C) G3/G3-DOTA-Cy5.5-PS and (D) P-G2.5/G3-DOTA-Cy5.5-PS.

G3-DOTA-Cy5.5-PS CSTDs do not seem to show significant changes after they were, respectively, dispersed in water, phosphate buffered saline (PBS), or cell culture medium (DMEM with 10% FBS) for at least one week, suggesting their good colloidal stability.

Cytotoxicity and cellular uptake assays

Next, we investigated the cytocompatibility of the two constructed CSTDs. The viability of normal cells (L929 cells, a mouse fibroblast cell line) and cancer cells (B16 cells, a murine melanoma cell line) after treatment with P-G2.5/G3-DOTA-Cy5.5-PS or G3/G3-DOTA-Cy5.5-PS at different concentrations (0–5000 nM) was evaluated by a CCK-8 assay. The L929 cell viability could remain at 89% or above when treated with the P-G2.5/G3-DOTA-Cy5.5-PS or G3/G3-DOTA-PS-Cy5.5 CSTDs at a concentration as high as 5000 nM, showing the good cytocompatibility of both CSTDs (Fig. S7†). Apparently, both P-G2.5/G3-DOTA-Cy5.5-PS and G3/G3-DOTA-PS-Cy5.5 CSTDs show no toxicity to B16 cells at the tested concentrations, and the B16 cell viability remained at 88.51% and 91.58% after being incubated for 24 h at the highest tested concentration of 5000 nM (Fig. S8†).

To confirm the cellular uptake of the CSTDs by B16 cells, flow cytometry was first employed to detect B16 cells incubated with P-G2.5/G3-DOTA-Cy5.5-PS or G3/G3-DOTA-Cy5.5-PS CSTDs at different Cy5.5 concentrations (0.5, 1, 2, and 5 μM, respectively) for 4 h. Obviously, B16 cells treated with both CSTDs showed an increased fluorescence intensity with an increase in CSTD concentration when compared to the PBS control group (Fig. 2A and Fig. S9†). It is noted that the fluorescence intensity of Cy5.5 in B16 cells is much higher in the P-G2.5/G3-DOTA-Cy5.5-PS group than in the G3/G3-DOTA-Cy5.5-PS group at the same Cy5.5 concentrations (Fig. 2B). The fluorescence intensities of the P-G2.5/G3-DOTA-Cy5.5-PS group are 1.61, 2.15, and 1.88 times higher than those of the G3/G3-DOTA-Cy5.5-PS group at the same respective Cy5.5 concentrations ($p < 0.001$). Confocal laser scanning microscopy (CLSM) was next adopted to investigate the intracellular uptake of the CSTDs by B16 cells (Fig. 2C). When incubated with P-G2.5/G3-DOTA-Cy5.5-PS, a more significant red fluorescence signal can be observed in B16 cells than for the G3/G3-DOTA-Cy5.5-PS and PBS groups, which is consistent with the results of flow cytometry. Overall, the P-G2.5/G3-DOTA-Cy5.5-PS CSTDs have a better cellular uptake and internalization tendency than the *soft* counterpart, which is beneficial for enhanced tumor imaging.

Deep penetration in B16 tumor spheroids *in vitro*

A 3D multicellular tumor spheroid (MCTS) model which simulates the tumor microenvironment and the solid tumor 3D space *in vivo* was utilized to study the penetration of G3/G3-DOTA-Cy5.5-PS and P-G2.5/G3-DOTA-Cy5.5-PS. We first prepared a B16 3D MCTS model with a diameter of about 300 μm, which was then incubated with the G3/G3-DOTA-Cy5.5-PS and

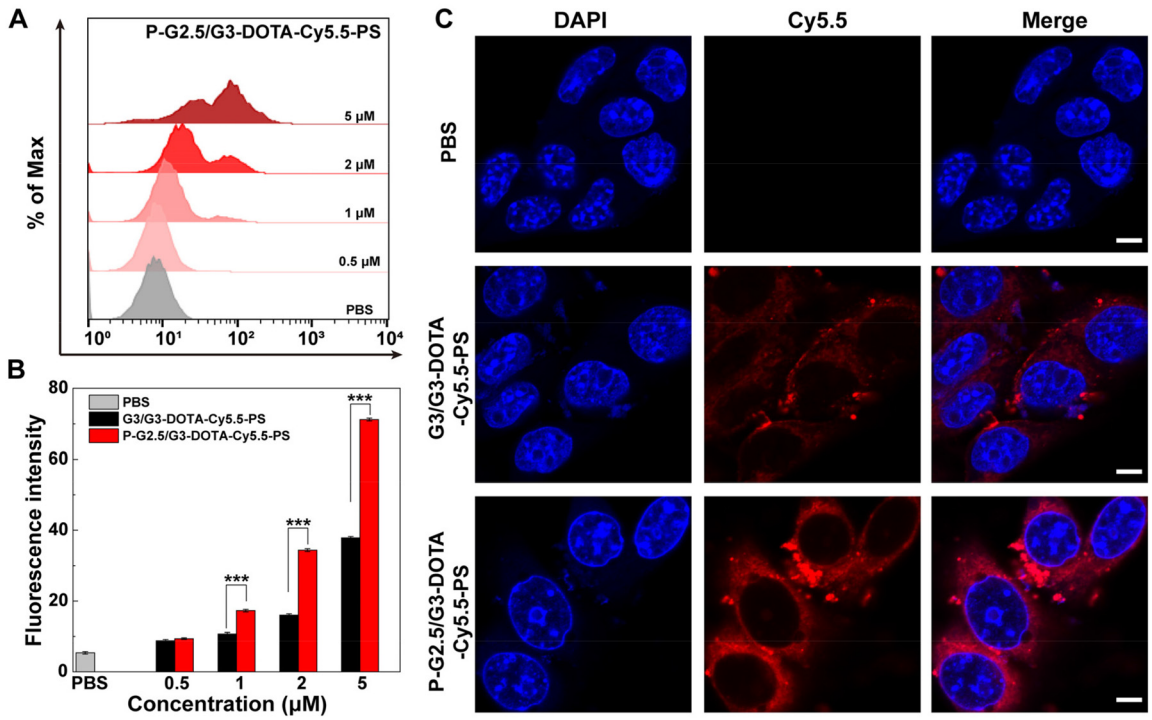

Fig. 2 (A) Fluorescence intensity histograms of Cy5.5 in B16 cells after being incubated with P-G2.5/G3-DOTA-Cy5.5-PS at different Cy5.5 concentrations (0.5, 1, 2, and 5 μM, respectively) for 4 h. (B) Quantitative analysis of the fluorescence intensity of Cy5.5 in B16 cells after being incubated with G3/G3-DOTA-Cy5.5-PS or P-G2.5/G3-DOTA-Cy5.5-PS at various Cy5.5 concentrations for 4 h. (C) CLSM observation of B16 cells after being treated with G3/G3-DOTA-Cy5.5-PS or P-G2.5/G3-DOTA-Cy5.5-PS ([Cy5.5] = 5 μM, scale bar = 5 μm for each panel). For B, ***$p < 0.001$ ($n = 3$).

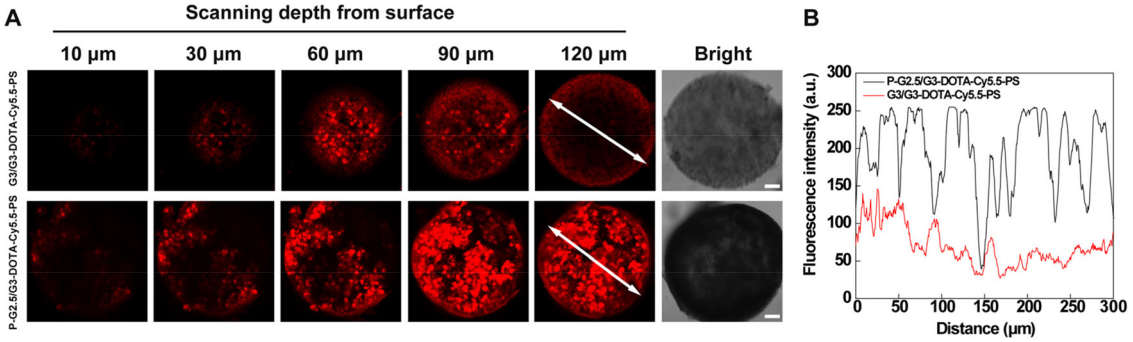

Fig. 3 (A) CLSM images of 3D B16 MCTS incubated with G3/G3-DOTA-Cy5.5-PS and P-G2.5/G3-DOTA-Cy5.5-PS for 6 h ([Cy5.5] = 5 μM for both materials, scale bar = 50 μm for each panel). (B) The fluorescence intensity profile (source: white arrow line in A) of B16 3D MCTS incubated with G3/G3-DOTA-Cy5.5-PS and P-G2.5/G3-DOTA-Cy5.5-PS for 6 h.

P-G2.5/G3-DOTA-Cy5.5-PS CSTDs, respectively. After incubation for 6 h, CLSM was used to observe the penetration of CSTDs (Fig. 3). It is clear that the B16 3D MCTSs treated with P-G2.5/G3-DOTA-Cy5.5-PS display a significant red fluorescence signal spread throughout the whole spheroid, while a relatively low fluorescence signal of MCTSs is seen in the G3/G3-DOTA-Cy5.5-PS group, suggesting a stronger tumor penetration capacity of P-G2.5/G3-DOTA-Cy5.5-PS than that of G3/G3-DOTA-Cy5.5-PS (Fig. 3A). As shown in Fig. 3B, the fluorescence intensity in the middle section of the B16 MCTS after treatment with P-G2.5/G3-DOTA-Cy5.5-PS is much higher than that after treatment with G3/G3-DOTA-Cy5.5-PS. The better tumor penetration of the P-G2.5/G3-DOTA-Cy5.5-PS CSTDs than that of the G3/G3-DOTA-Cy5.5-PS CSTDs should be attributed to the greater rigidity of the former than that of the latter, in line with the literature.[15]

Fluorescence imaging of a subcutaneous melanoma model *in vivo*

First of all, the hemocompatibility of P-G2.5/G3-DOTA-Cy5.5-PS was evaluated by a hemolytic assay before subsequent *in vivo* experiments. After incubation with the P-G2.5/G3-DOTA-Cy5.5-PS CSTDs at different concentrations, the hemolysis rates of mouse erythrocytes are all lower than the threshold value of 5%, suggesting the excellent hemocompatibility of the CSTDs (Fig. S10†). Next, we evaluated the potential to employ the P-G2.5/G3-DOTA-Cy5.5-PS CSTDs for tumor fluorescence imaging. First, each B16 tumor-bearing mouse was intravenously injected with the CSTDs at a Cy5.5 concentration of 5 μM, and then the fluorescence images were collected at different time points postinjection (Fig. 4A). The fluorescence signals of tumor sites first increased and then decreased with time postinjection for both G3/G3-DOTA-Cy5.5-PS and P-G2.5/G3-DOTA-Cy5.5-PS groups. Notably, the peak tumor fluorescence intensity was achieved at 1 h postinjection for both CSTDs, and the fluorescence intensity of the P-G2.5/G3-DOTA-Cy5.5-PS group was 1.45 times higher than that of the G3/G3-DOTA-Cy5.5-PS group at the peak time point. Further quantitative analysis presented in Fig. 4B shows that a more significant tumor fluorescence signal can be obtained in the P-G2.5/G3-DOTA-Cy5.5-PS group than in the G3/G3-DOTA-Cy5.5-PS group at all studied time points ($p < 0.01$). The reason behind this could be the more *rigid* structure of P-G2.5/G3-DOTA-Cy5.5-PS CSTDs than that of the *soft* counterpart G3/G3-DOTA-Cy5.5-PS, which likely amplifies the tumor EPR effect for better tumor accumulation.

In order to analyze the metabolism of P-G2.5/G3-DOTA-Cy5.5-PS CSTDs *in vivo*, the tumor-bearing mice were sacrificed at 12 h postinjection to observe the fluorescence distribution in the major organs (heart, liver, spleen, lungs, and kidneys) and tumors. As displayed in Fig. 4C and D, a much stronger fluorescence signal in the tumor tissue can be found in the P-G2.5/G3-DOTA-Cy5.5-PS group than in the G3/G3-DOTA-Cy5.5-PS group, in alignment with *in vivo* live-body imaging results. Furthermore, a stronger fluorescence intensity in the spleen and kidneys can be seen in the G3/G3-DOTA-Cy5.5-PS group than in the P-G2.5/G3-DOTA-Cy5.5-PS group ($p < 0.01$), while a weaker fluorescence intensity in the liver can be observed in the G3/G3-DOTA-Cy5.5-PS group than in the P-G2.5/G3-DOTA-Cy5.5-PS group ($p < 0.05$, Fig. S11†). Our results suggest a more effective tumor accumulation capability of the *rigid* P-G2.5/G3-DOTA-Cy5.5-PS CSTDs than that of the *soft* counterpart G3/G3-DOTA-Cy5.5-PS. Obviously, both types of CSTDs show strong fluorescence signals in the kidneys with weak fluorescence distribution in other organs at 12 h postinjection, revealing that the CSTDs can be mainly metabolized and eliminated from the body through the kidneys.

SPECT imaging of tumors *in vivo*

SPECT, which is characterized by the specific display of the blood flow, function and metabolic changes in organs or lesions, facilitates early and specific diagnosis of various diseases including malignant tumors, Alzheimer's disease and epilepsy.[37–39] Meanwhile, SPECT imaging can be utilized to directly observe the distribution of ^{99m}Tc-labeled nanomaterials and investigate the radioactivity of specific organs and tumors. In order to analyze the SPECT imaging potential

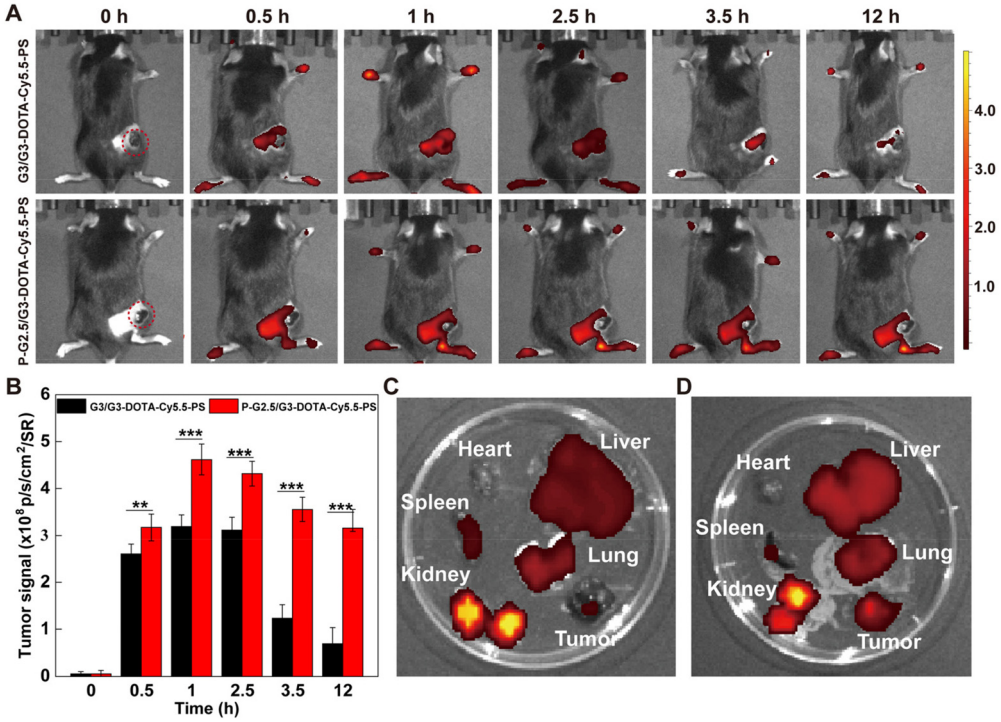

Fig. 4 (A) Fluorescence images of B16 tumor-bearing mice after intravenous injection of G3/G3-DOTA-Cy5.5-PS or P-G2.5/G3-DOTA-Cy5.5-PS at different time points (0, 0.5, 1, 2.5, 3.5, and 12 h, respectively). (B) The quantification of fluorescence signals of tumors removed from mice at different time points postinjection. The fluorescence imaging of major organs (heart, liver, spleen, lungs, and kidneys) and tumors from the mice intravenously injected with G3/G3-DOTA-Cy5.5-PS (C) or P-G2.5/G3-DOTA-Cy5.5-PS (D) after 12 h. For B, $^{**}p < 0.01$ and $^{***}p < 0.001$, respectively ($n = 3$).

of the CSTDs, G3/G3-DOTA-Cy5.5-PS and P-G2.5/G3-DOTA-Cy5.5-PS CSTDs were labeled with ^{99m}Tc with a labeling efficiency of 83.33 ± 2.98% and 62.34 ± 4.16%, respectively, and they displayed excellent radio stability as demonstrated by evaluation of their radiochemical purities at different time points (Table S2†). B16 tumor-bearing mice were intravenously injected with ^{99m}Tc-P-G2.5/G3-DOTA-Cy5.5-PS or ^{99m}Tc-G3/G3-DOTA-Cy5.5-PS, and SPECT imaging was performed at different time points postinjection (30, 60, 90, 150, or 210 min). As displayed in Fig. 5A, both groups show very similar SPECT signals distributed over the tumor and bladder sites at 30–90 min postinjection, while the SPECT signal intensity at the tumor site injected with ^{99m}Tc-P-G2.5/G3-DOTA-Cy5.5-PS is much higher than that at the tumor site injected with ^{99m}Tc-G3/G3-DOTA-Cy5.5-PS for all studied time points. In the ^{99m}Tc-G3/G3-DOTA-Cy5.5-PS group, the SPECT signal at the tumor site declines significantly at 150–210 min postinjection, and the distribution of the SPECT signal at the bladder site also decreases, demonstrating that ^{99m}Tc-G3/G3-DOTA-Cy5.5-PS can be gradually cleared from the bladder and excreted out of the body. In contrast, significant SPECT signals can be observed at the tumor sites and bladders in the ^{99m}Tc-P-G2.5/G3-DOTA-Cy5.5-PS group at 30–210 min postinjection, suggesting that ^{99m}Tc-P-G2.5/G3-DOTA-Cy5.5-PS could be successfully retained at the tumor site due to the enhanced EPR effect with extended kidney metabolization and clearance.

Quantification of the SPECT signal at the tumor site shows a trend of first increase and then decrease over time postinjection, and a peak SPECT signal at 60 min postinjection can be seen for both groups (Fig. 5B). The tumor SPECT signal in the ^{99m}Tc-P-G2.5/G3-DOTA-Cy5.5-PS group is much higher than that in the ^{99m}Tc-G3/G3-DOTA-Cy5.5-PS group at different time points ($p < 0.001$), which is consistent with the results of fluorescence imaging *in vivo*. These results indicate that the enhanced EPR effect and effective escape from phagocytosis of the RES of the ^{99m}Tc-P-G2.5/G3-DOTA-Cy5.5-PS CSTDs should stem from their increased rigidity and antifouling ability in comparison with the *soft* counterpart.

To assess the metabolic behavior of ^{99m}Tc-P-G2.5/G3-DOTA-Cy5.5-PS, B16 tumor-bearing mice intravenously injected with the two CSTDs were sacrificed at different time points postinjection (30, 90, 150 or 210 min, respectively). The radioactivity levels in the major organs and tumors were measured using a γ-counter (Fig. S12†). The radioactivity of tumors in the ^{99m}Tc-P-G2.5/G3-DOTA-Cy5.5-PS group is stronger than that in the ^{99m}Tc-G3/G3-DOTA-Cy5.5-PS group at 90 min post injection, in good agreement with the *in vivo* SPECT imaging results ($p < 0.01$, Fig. S13†). Clearly, the highest radioactivity distribution was obtained in the kidneys compared with other organs, revealing that the two CSTDs are finally metabolized mainly through the kidneys.

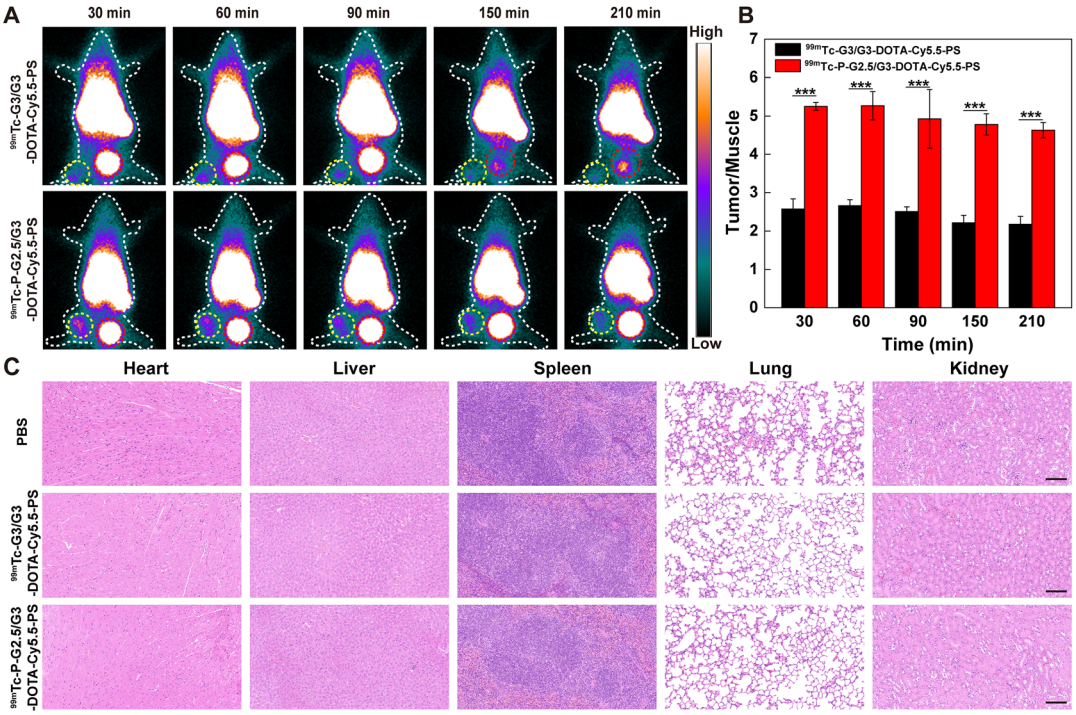

Fig. 5 (A) SPECT imaging of B16 tumor-bearing mice after being intravenously injected with ^{99m}Tc-P-G2.5/G3-DOTA-Cy5.5-PS or ^{99m}Tc-G3/G3-DOTA-Cy5.5-PS at different time points (30, 60, 90, 150, or 210 min, respectively). The yellow and red circles represent the tumors and bladders, respectively. (B) Quantification of tumor SPECT signals in the ^{99m}Tc-G3/G3-DOTA-Cy5.5-PS and ^{99m}Tc-P-G2.5/G3-DOTA-Cy5.5-PS groups at different time points. (C) Representative hematoxylin & eosin (H&E)-stained sections of the major organs of tumor-bearing mice after different treatments for 7 days. The scale bar for each panel represents 100 μm. For B, ***$p < 0.001$ ($n = 3$).

In vivo biosafety investigation

The *in vivo* biosafety of the two types of CSTDs was next validated. Each healthy mouse was injected with ^{99m}Tc-P-G2.5/G3-DOTA-Cy5.5-PS or ^{99m}Tc-G3/G3-DOTA-Cy5.5-PS at 5 mg kg^{-1} *via* the tail vein and sacrificed at 7 days postinjection. The major organs including the heart, liver, spleen, lungs, and kidneys were extracted and sectioned for H&E staining to observe the histological changes. As displayed in Fig. 5C, mice treated with both ^{99m}Tc-P-G2.5/G3-DOTA-Cy5.5-PS and ^{99m}Tc-G3/G3-DOTA-Cy5.5-PS do not appear to produce significant cardiotoxicity, liver damage, hepatotoxicity, spleen infiltration and lung enlargement, which is similar to normal organs in the PBS group. This demonstrates the robust biosafety of the prepared ^{99m}Tc-P-G2.5/G3-DOTA-Cy5.5-PS and ^{99m}Tc-G3/G3-DOTA-Cy5.5-PS CSTDs with great potential for fluorescence and SPECT dual-mode imaging of tumors *in vivo*.

Conclusions

In summary, we developed phosphorus CSTDs with *rigid* cores as a promising platform for enhanced tumor imaging through an amplified EPR effect. The P-G2.5/G3 CSTDs can be sequentially modified with DOTA for ^{99m}Tc labeling, Cy5.5 for fluorescence imaging, and 1,3-PS for acquiring antifouling property. In comparison with the *soft* counterpart material G3/G3-DOTA-Cy5.5-PS with the same antifouling property and cytocompatibility, the created P-G2.5/G3-DOTA-Cy5.5-PS CSTDs display improved cellular uptake, internalization tendency, and 3D tumor spheroid penetration ability, thus enabling enhanced fluorescence and SPECT (after being labelled with ^{99m}Tc) dual-mode tumor imaging through the amplified EPR effect. Our study suggests that the rigidity of the CSTDs matters in terms of the improved EPR effect and enhanced tumor imaging capability. The developed phosphorus CSTDs with *rigid* cores may be adapted for a variety of cancer nanomedicine applications.

Author contributions

Mengsi Zhan: formal analysis, investigation, data curation, validation, and writing – original draft. Dayuan Wang: methodology, formal analysis, validation, and data curation. Lingzhou Zhao: methodology, formal analysis, and data curation. Liang Chen: formal analysis and data curation. Zhijun Ouyang: formal analysis and data curation. Serge Mignani: formal analysis and resources. Jean-Pierre Majoral: formal analysis and resources. Jinhua Zhao: resources and funding acquisition. Guixiang Zhang: resources, funding acquisition, and project administration. Xiangyang Shi: conceptualization, resources, funding acquisition, project administration, supervision, and writing – review and editing. Mingwu Shen: formal analysis,

software, resources, funding acquisition, project administration, supervision, and writing – review and editing.

Conflicts of interest

The authors declare no competing financial interest.

Acknowledgements

This study was financially supported by the Science and Technology Commission of Shanghai Municipality (21490711500, 23WZ2503300, 20520710300 and 20DZ2254900), the National Key R&D Program (2022YFE0196900), the Shanghai Education Commission through the Leading Talent Program and the Fundamental Research Funds for the Central Universities and Graduate Student Innovation Fund of Donghua University (CUSF-DH-D-2023054). X.S. also acknowledged the support by FCT-Fundação para a Ciência e a Tecnologia through the CQM Base Fund - UIDB/00674/2020, and Programmatic Fund - UIDP/00674/2020, and by ARDITI-Agência Regional para o Desenvolvimento da Investigação Tecnologia e Inovação through funds from Região Autónoma da Madeira-Governo Regional.

References

1 H. Wang, S. Q. Lin, S. L. Wang, Z. X. Jiang, T. H. Ding, X. L. Wei, Y. Lu, F. Yang and C. Y. Zhan, *Nano Lett.*, 2022, **22**, 6516–6522.
2 J. J. Liu, G. M. Li, H. H. Guo, C. Ni, Y. Gao, X. Y. Cao, J. D. Xia, X. Y. Shi and R. Guo, *ACS Appl. Mater. Interfaces*, 2023, **15**, 12809–12821.
3 Y. M. Zhang, Z. J. Ouyang, M. S. Zhan, R. Yang, Y. Gao, L. L. Li, R. Guo, X. Y. Shi and X. Y. Cao, *Small*, 2023, **19**, 2301914.
4 H. X. Liu, C. M. Mei, X. R. Deng, W. Q. Lin, L. Z. He and T. F. Chen, *Biomaterials*, 2021, **264**, 120434.
5 I. Biancacci, F. De Lorenzi, B. Theek, X. Y. Bai, J. N. May, L. Consolino, M. Baues, D. Moeckel, F. Gremse, S. von Stillfried, A. El Shafei, K. Benderski, A. A. Shalmani, A. Wang, J. Momoh, Q. Pena, E. M. Buhl, J. Buyel, W. Hennink, F. Kiessling, J. Metselaar, Y. Shi and T. Lammers, *Adv. Sci.*, 2022, **9**, 2103745.
6 C. Caro, A. Avasthi, J. M. Paez-Munoz, M. P. Leal and M. L. Garcia-Martin, *Biomater. Sci.*, 2021, **9**, 7984–7995.
7 X. Luan, H. B. Yuan, Y. D. Song, H. X. Hu, B. Wen, M. He, H. X. Zhang, Y. Li, F. Li, P. Shu, J. P. Burnett, N. Truchan, M. Palmisano, M. P. Pai, S. Zhou, W. Gao and D. X. Sun, *Biomaterials*, 2021, **275**, 120910.
8 S. Y. Hua, J. He, F. P. Zhang, J. H. Yu, W. X. Zhang, L. Y. Gao, Y. Y. Li and M. Zhou, *Biomaterials*, 2021, **268**, 120590.
9 W. J. Liu, L. Y. Zhang, Z. R. Dong, K. H. Liu, H. S. He, Y. Lu, W. Wu and J. P. Qi, *Nano Res.*, 2022, **15**, 9243–9252.
10 M. Souri, M. Soltani, F. M. Kashkooli, M. K. Shahvandi, M. Chiani, F. S. Shariati, M. R. Mehrabi and L. L. Munn, *Mater. Today Bio*, 2022, **13**, 100208.
11 J. J. Chen, Z. Y. Jiang, Y. S. Zhang, J. X. Ding and X. S. Chen, *Appl. Phys. Rev.*, 2021, **8**, 041321.
12 J. Chen, T. Chen, Q. Fang, C. Pan, O. U. Akakuru, W. Ren, J. Lin, A. Sheng, X. Ma and A. Wu, *Exploration*, 2022, **2**, 20220014.
13 Y. J. He, X. J. Tian, X. Y. Fan, X. Y. Gong, S. W. Tan, A. Q. Pan, S. Q. Liang, H. Xu and F. F. Zhou, *ACS Appl. Mater. Interfaces*, 2023, **15**, 552–565.
14 C. Song, Z. J. Ouyang, H. H. Guo, J. Qu, Y. Gao, J. D. Xia, M. W. Shen and X. Y. Shi, *Biomacromolecules*, 2021, **22**, 2181–2188.
15 Y. B. Liu, K. M. C. Bravo and J. W. Liu, *Nanoscale Horiz.*, 2021, **6**, 78–94.
16 Z. Dai, M. R. Yu, X. Yi, Z. M. Wu, F. L. Tian, Y. Q. Miao, W. Y. Song, S. F. He, E. Ahmad, S. Y. Guo, C. L. Zhu, X. X. Zhang, Y. M. Li, X. H. Shi, R. Wang and Y. Gan, *ACS Nano*, 2019, **13**, 7676–7689.
17 J. S. Sun, L. Zhang, J. L. Wang, Q. Feng, D. B. Liu, Q. F. Yin, D. Y. Xu, Y. J. Wei, B. Q. Ding, X. H. Shi and X. Y. Jiang, *Adv. Mater.*, 2015, **27**, 1402–1407.
18 X. H. Sun, T. Nomoto, H. Takemoto, M. Matsui, H. C. Guo, Y. D. Sun, Y. Miura and N. Nishiyama, *J. Controlled Release*, 2021, **329**, 513–523.
19 M. Eguchi, S. Hirata, I. Ishigami, N. Shuwari, R. Ono, M. Tachibana, M. Tanuma, A. Kasai, H. Hashimoto, K. Ogawara, H. Mizuguchi and F. Sakurai, *J. Controlled Release*, 2023, **354**, 35–44.
20 J. P. He, J. Z. Chen, S. L. Lin, D. C. Niu, J. N. Hao, X. B. Jia, N. Li, J. L. Gu, Y. S. Li and J. L. Shi, *Biomacromolecules*, 2018, **19**, 2923–2930.
21 J. Y. Liu, Z. J. Xiong, J. L. Zhang, C. Peng, B. Klajnert-Maculewicz, M. W. Shen and X. Y. Shi, *ACS Appl. Mater. Interfaces*, 2019, **11**, 15212–15221.
22 Z. J. Xiong, Y. Wang, W. Zhu, Z. J. Ouyang, Y. Zhu, M. W. Shen, J. D. Xia and X. Y. Shi, *Small Methods*, 2021, **5**, 2100204.
23 C. Song, M. S. Zhan, Z. J. Ouyang, Y. G. Yao, Y. Gao, M. W. Shen and X. Y. Shi, *J. Controlled Release*, 2023, **358**, 601–611.
24 Y. Gao, Z. J. Ouyang, C. Yang, C. Song, C. J. Jiang, S. L. Song, M. G. Shen and X. Y. Shi, *Adv. Healthcare Mater.*, 2021, **10**, 2100833.
25 M. S. Zhan, J. R. Qiu, Y. Fan, L. Chen, Y. Q. Guo, Z. Q. Wang, J. Li, J. P. Majoral and X. Y. Shi, *Adv. Mater.*, 2023, **35**, 2208277.
26 J. Li, L. Chen, C. S. Li, Y. Fan, M. S. Zhan, H. X. Sun, S. Mignani, J. P. Majoral, M. W. Shen and X. Y. Shi, *Theranostics*, 2022, **12**, 3407–3419.
27 J. R. Qiu, L. Chen, M. S. Zhan, R. Laurent, J. Bignon, S. Mignani, X. Y. Shi, A. M. Caminade and J. P. Majoral, *Bioconjugate Chem.*, 2021, **32**, 339–349.

28 C. Song, Y. C. Xiao, Z. J. Ouyang, M. W. Shen and X. Y. Shi, *J. Mater. Chem. B*, 2020, **8**, 2768–2774.
29 Q. Hu, J. Y. Yao, X. Q. Wang, Y. F. Wang, X. L. Fu, J. Ma, H. Lin, J. Q. Xu, L. H. Shen and X. B. Yu, *ACS Appl. Mater. Interfaces*, 2022, **14**, 8782–8792.
30 D. Y. Wang, L. Chen, Y. Gao, C. Song, Z. J. Ouyang, C. S. Li, S. Mignani, J. P. Majoral, X. Y. Shi and M. W. Shen, *J. Mater. Chem. B*, 2021, **9**, 6149–6154.
31 Y. Du, Y. Huo, Q. Yang, Z. Han, L. Hou, B. Cui, K. Fan, Y. Qiu, Z. Chen, W. Huang, J. Lu, L. Cheng, W. Cai and L. Kang, *Exploration*, 2023, **3**, 20220041.
32 F. Lu, R. Y. Sang, Y. Tang, H. Xia, J. W. Liu, W. Huang, Q. L. Fan and Q. Wang, *Acta Biomater.*, 2022, **151**, 528–536.
33 J. W. Liu, Y. W. Xiong, Y. C. Gao, X. P. Xu, K. Chen, Q. M. Shen, W. Huang, Q. L. Fan and Q. Wang, *Small*, 2023, **19**, 2205640.
34 W. Zhang, I. Oraiqat, H. Lei, P. L. Carson, I. Ei Naqa and X. Wang, *BME Front.*, 2020, **2020**, 9853609.
35 X. L. Zhang, M. Zhao, L. Wen, M. R. Wu, Y. Yang, Y. J. Zhang, Y. Wu, J. Zhong, H. B. Shi, J. F. Zeng, G. L. Wang and M. Y. Gao, *Biomater. Sci.*, 2021, **9**, 3069–3075.
36 J. M. Zhang, L. J. Yang, F. Huang, C. Zhao, J. J. Liu, Y. M. Zhang and J. F. Liu, *Adv. Healthcare Mater.*, 2021, **10**, 2101190.
37 X. Zhou, N. Yan, E. J. Cornel, H. D. Cai, S. B. Xue, H. Xi, Z. Fan, S. S. He and J. Z. Du, *Biomaterials*, 2021, **269**, 120345.
38 F. P. M. Oliveira, Z. Walker, R. W. H. Walker, J. Attems, J. C. Castanheira, A. Silva, C. Oliveira, S. Vaz, M. Silva and D. C. Costa, *J. Neurol., Neurosurg. Psychiatry*, 2021, **92**, 662–667.
39 Z. Li, W. B. Sun, W. J. Duan, Y. Q. Jiang, M. Chen, G. R. Lin, Q. Y. Wang, Z. Fan, Y. S. Tong, L. Chen, J. N. Li, G. L. Cheng, C. Wang, C. Li and L. Chen, *ACS Appl. Mater. Interfaces*, 2022, **15**, 14–25.